THE JOURNAL OF PHYSICAL CHEMISTRY C
A JOURNAL OF THE AMERICAN CHEMICAL SOCIETY

pubs.acs.org/JPCC

Article

Improved Charge Transport in PbS Quantum Dot Thin Films following Gel Permeation Chromatography Purification

Fiaz Ahmed, Mathew L. Kelley, MVS Chandrashekhar, and Andrew B. Greytak*

Cite This: *J. Phys. Chem. C* 2021, 125, 17796–17805

Read Online

ACCESS | Metrics & More | Article Recommendations | Supporting Information

ABSTRACT: We report a systematic investigation of the electronic properties of lead sulfide quantum dot (QD) films prepared by gel permeation chromatography (GPC) or conventional precipitation/redispersion (PR) to identify the effect of these different purification methods. Following spin coating and ligand exchange with ethanedithiol, metal top contacts were patterned by evaporation through a shadow mask. A transmission line model (TLM) approach was employed to separate the bulk resistivity from the contact resistance. The GPC-purified film showed a resistivity as low as 1.5 kΩ-cm, ∼3× lower than for PR, as well as decreased contact resistance with Au contacts. These differences in electronic properties were accompanied by decreased surface roughness. By tuning the workfunction of metal contacts to these films, a transition from ohmic to rectifying behavior characteristic of *p*-type conductivity was observed. The contrasting behavior of the ohmic- and Schottky-contacted devices permits estimation of majority carrier (hole) and minority carrier (electron) properties, respectively. With ohmic contacts, the GPC-purified film displayed an increased responsivity (>10 mA/W) and photoconductive gain along with a decrease in photocurrent lifetimes, indicating improved mobility. Scanning photocurrent microscopy (SPCM) was used to characterize the minority carrier diffusion length in Schottky-contacted devices, which was found to be comparable in all three films studied, but a much shorter photocurrent lifetime in the GPC-purified film indicates a much greater electron mobility, indicative of diminished trapping. The results indicate that film properties are sensitive to preparation conditions in addition to ligand density and that GPC is a highly effective route to QDs suited for optoelectronic applications.

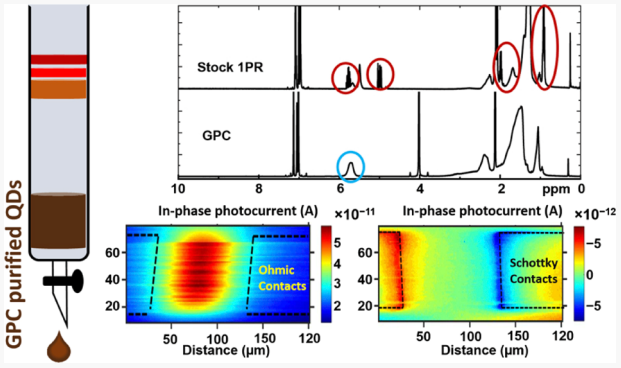

INTRODUCTION

The desire to incorporate improved and broadly deployable photodetectors and photovoltaics in daily life has fueled the hunt for new materials that enable simple design and fabrication techniques for low-cost, flexible, and large area semiconductor devices.[1−3] Semiconducting colloidal quantum dots (QDs), which are zero-dimensional, nanoscale crystals of analogous bulk semiconductors, offer a versatile platform for engineering photovoltaic devices, displays, and flexible electronics.[4−6] QDs are promising semiconducting materials for electronic and optoelectronic devices due to tunable size-dependent bandgaps, multi-exciton generation, and high achievable quantum efficiencies.[7,8]

In traditional solution-based synthesis of QDs, long-chain organic ligands (e.g., oleate) are used as surface capping agents to preserve size and prevent aggregation.[7,9] Great efforts have been made to find suitable short-chain surface ligands to reduce spacing between adjacent QDs and improve charge transport in optoelectronic devices.[10−13] To build devices out of QDs, post-synthesis reaction byproducts and residual precursors are removed by multiple precipitation and redissolution (PR) cycles. The PR technique uses polar anti-solvents that can promote QD aggregation.[14] Multiple PR cycles result in loss of native ligands bound to the surface, which can induce surface traps that degrade the optoelectronic performance of the dots.[15−19] Ligands also inhibit coalescence, which has been shown to lead to electronic traps in QD films.[20] This presents a tradeoff between QD agglomeration and removal of reaction byproducts and residual precursors through multiple PR cycles. Our group has shown that post-synthesis purification of QDs by gel permeation chromatography (GPC) can break this tradeoff.[21−24] GPC is an effective way to separate analytes on the basis of size, through which larger particles elute faster than smaller ones. It effectively separates QDs from byproducts and unreacted precursors while reproducibly preserving ligand surface termination. GPC also prevents agglomeration by keeping QDs dispersed in a homogeneous solvent environment during purification. Post-

Received: May 12, 2021
Revised: July 26, 2021
Published: August 10, 2021

https://doi.org/10.1021/acs.jpcc.1c04218
J. Phys. Chem. C 2021, 125, 17796−17805

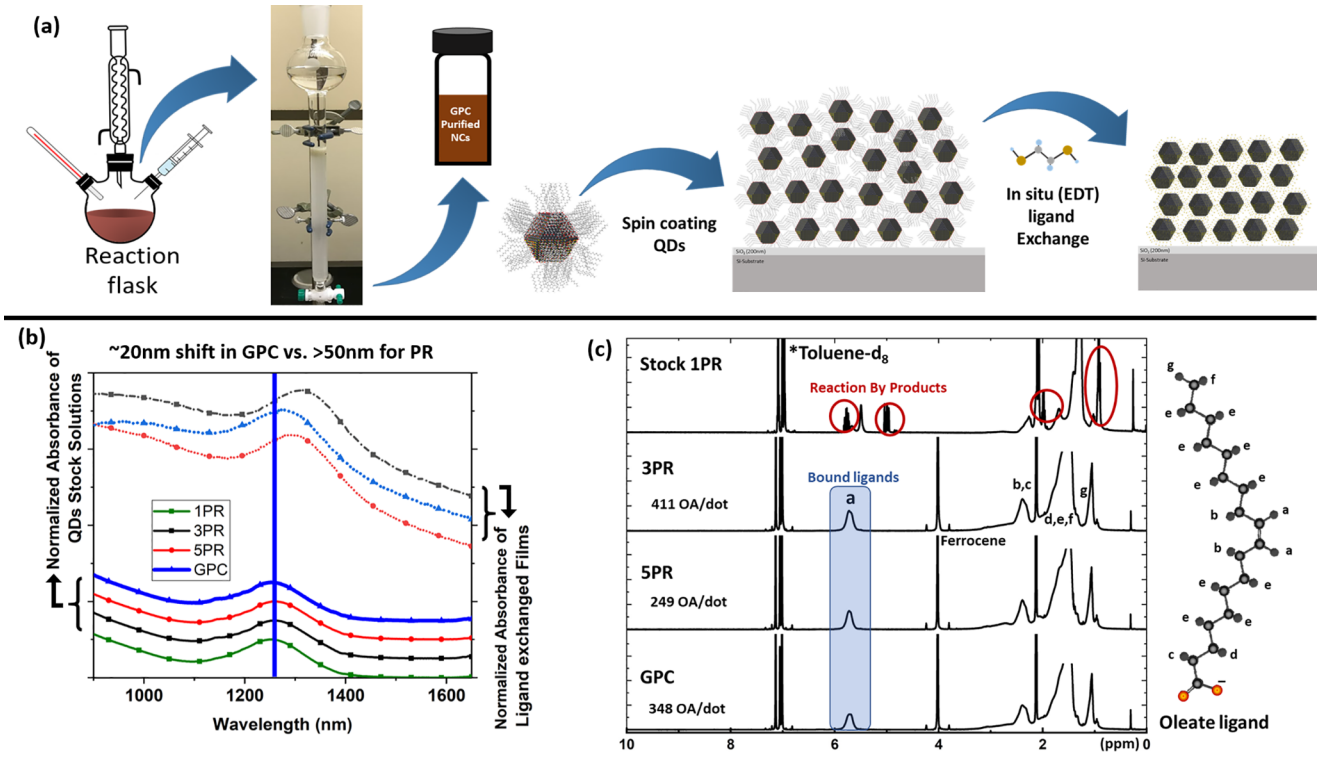

Figure 1. (a) Synthesis and purification route for the layer-by-layer spin coating and ligand exchange process used to make a compact QD film. (b) Absorbance of QDs after synthesis, purified solutions, and ligand exchanged films. (c) ^{1}H NMR spectrum of Stock (1PR) and purified (3PR, 5PR, and GPC) QD solutions.

synthesis purification steps are particularly crucial in film fabrication via solid-state ligand exchange (SSLE), where diffusion of ligands, impurities, and QDs is limited within the deposited film.[25] While GPC-purified QDs have been employed in electronic devices, film electronic properties including conductivity, photoconductivity, and photocurrent lifetimes have not been directly examined in SSLE films prepared following GPC or compared to similar films prepared following PR. Such comparisons are necessary as effective purification strategies could help eliminate factors such as cracks, surface traps, and coalescence of QDs that degrade QD film performance.

Because PbS QDs offer effective bandgaps tunable across the shortwave to near-infrared range and synthetic methods with good control of size distributions have been developed, PbS QDs have been intensely studied as a model platform for colloidal QD optoelectronics.[4,26,27] For example, spin-casting of oleate-coated PbS QDs followed by ligand exchange with ethanedithiol (EDT) can be used to build films with *p*-type character that can be employed in representative Schottky barrier and oxide heterojunction photovoltaic devices.[28] A variety of techniques have been applied to learn material properties (such as carrier type, density, mobility, and lifetime) and interfacial properties (such as contact resistance and contact potentials) that govern device performance and how these properties can be influenced and improved by attention to preparative techniques. Many of these studies focus on vertical device architectures common to thin-film photovoltaics.[29−32] While clearly advantageous for many applications, vertical architectures present some limitations for isolating the behavior of individual junctions. Lateral transport devices, in which current moves in the plane of the thin film, have been investigated primarily in field-effect transistor studies[28,33] that permit measurement of majority carrier mobility at high carrier densities that may not be representative of excited-state carrier dynamics in optoelectronic devices. However, lateral transport devices also provide the opportunity to separate junction behavior from bulk properties through varying contact separation in transmission line model (TLM) studies[34] and through localized photocurrent and photovoltage measurements at metal−semiconductor interfaces.[33,35,36] For example, scanning photocurrent microscopy (SPCM) has been used by Law et al.[35] to characterize the effect of gating on minority carrier diffusion length in PbSe QD FETs and by Strasfeld et al.[36] to resolve ohmic and Schottky contacts to PbS QD films. The former examples use films deposited over pre-patterned bottom contacts, but this can lead to uneven film thickness and one study found that top contacts exhibited significantly lower contact resistance in TLM measurement of CdSe QD films.[34]

Here, we employ laterally patterned top contacts to directly compare the performance of PbS-EDT films prepared following GPC purification and conventional PR cycles in photoconductive and rectifying optoelectronic devices and to permit comparison to state-of-the-art literature results. The overall experimental approach for QD film formation by layer-by-layer spin coating and ligand exchange of GPC-purified PbS QDs is outlined in Figure 1a.

METHODS

QD Synthesis and Preparation. Oleate-capped PbS QDs, with the lowest energy electronic transition λ_{1s} of ∼1250 nm corresponding to a diameter of ∼4.4 nm, were synthesized through a previously described air-free synthetic route in 1-octadecene solvent,[37] and subsequent purification, film deposition, and ligand exchange steps were conducted in an

https://doi.org/10.1021/acs.jpcc.1c04218
J. Phys. Chem. C 2021, 125, 17796−17805

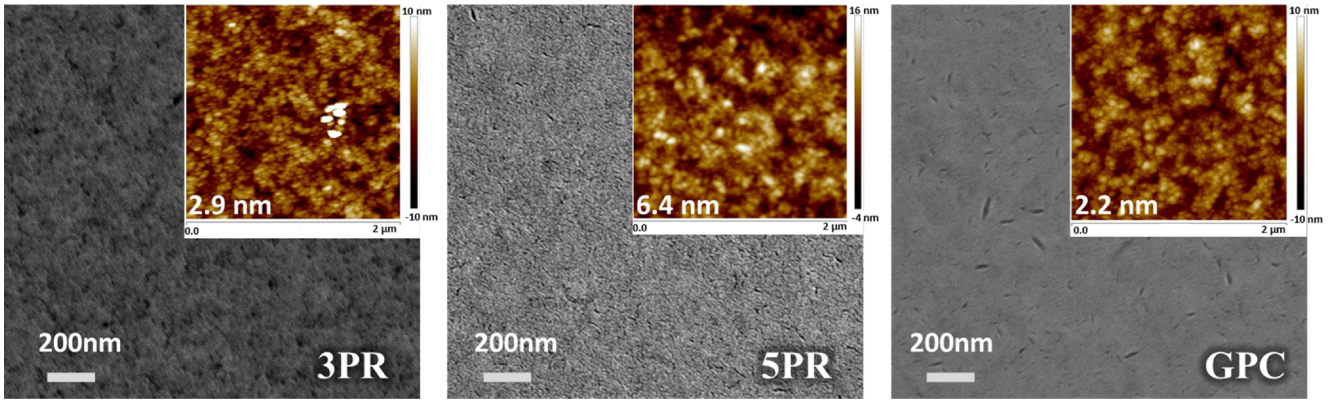

Figure 2. SEM surface morphology of films made using QDs purified by precipitation/redispersion (3PR and 5PR cycles) and the GPC technique. Insets are the AFM images of 2 μm × 2 μm area that shows surface profiles indicating the surface roughness.

inert atmosphere. Following synthesis and an initial precipitation under a nitrogen atmosphere using anhydrous methyl acetate (MeOAc, dried over activated 4 A molecular sieves), the QDs were redissolved in toluene to form a stock solution designated as 1PR.

A portion of QDs from the 1PR stock solution was brought through two further PR cycles, filtered through a 0.1 μm PTFE syringe filter, and brought to a final concentration of 25 mg/mL in anhydrous toluene (3PR). Similarly, a portion of the 3PR sample was brought through two further PR cycles (5PR). Separately, from the 1PR stock solution, 250 nmol of PbS QDs was purified by gel permeation chromatography (GPC).[23,38] The eluted fractions containing QDs were combined and concentrated by removing excess solvent under partial vacuum to achieve a final concentration of 25 mg/mL and then passed through a 0.1 μm filter to obtain the GPC sample used in subsequent work.

For GPC, the polystyrene gels (Bio-Beads S-X1, Bio-Rad) were prepared following Shen et al. (ref 38). In particular, beads were washed three times with an excess of toluene and swollen under ambient conditions in toluene for 24 h. These swollen beads were washed again with fresh toluene and then evacuated to dryness under Schlenk line vacuum before transferring into the glovebox. The beads were swollen a second time with anhydrous toluene inside the glovebox for another 24 h before loading onto the column as described previously. In a typical run, the 1PR aliquot was concentrated to a 200 μL volume under partial vacuum prior to injecting onto the column.

Film Fabrication. Conductive PbS QD films were formed on Si/SiO_2 substrates (wet oxidized, 200 nm thickness). Chips of ~1 cm^2 were cleaned by sequential sonication in acetone, isopropanol, ethanol, and DI water and finally dried under N_2 flow. Substrates were heated at 120 °C for 10 min to remove adsorbed water before transferring into the glovebox. QD films were deposited using a layer-by-layer deposition and ligand exchange process. Each coating cycle consisted of dropping 20 μL of PbS solution onto the substrate while spinning at 3000 rpm followed by treatment with 3 drops of 1.0% (v/v) 1,2-ethanedithiol in acetonitrile and rinsing with 3 drops of fresh acetonitrile and 3 drops of anhydrous toluene. Each deposition, ligand exchange, and cleaning step is 30 s apart and done in nitrogen-filled glovebox using a compact spin coater constructed from a hard drive motor and operated using an Arduino microcontroller. This coating cycle was repeated four times to get a ~100 nm-thick PbS QD film. Metal top contacts were evaporated through a shadow mask using an e-beam evaporator. The completed devices were then immediately tested for optoelectronic properties under normal atmosphere conditions using tungsten wire probe arms mounted on a scanning stage.

RESULTS AND DISCUSSION

Initial analysis of samples by ultraviolet−visible−near-infrared (UV−vis−NIR) absorption spectroscopy was used to monitor the lowest-energy electronic transition peak wavelengths, effective diameter according to a published calibration curve, and relative concentration. For these measurements, samples are diluted in *n*-octane under N_2. As shown in Figure 1b (full spectrum S1,S2), the different purification methods led to a minimal change in the absorption spectrum, indicating no great change in effective diameter or size distribution. However, UV−vis−NIR does not probe ligand populations associated with the QDs.

NMR is a standard and essential technique for the analysis of organic ligands on QD surfaces and the presence of unwanted impurities. Ligands attached to the surface of QDs characteristically exhibit broadened NMR spectral lines that can be distinguished on the basis of width and chemical shift from sharp peaks associated with freely diffusing small molecules.[39] The olefin resonance of oleate ligand species is well resolved from crowded aliphatic and aromatic protons associated with solvents and can be used to quantify total oleate concentration when ferrocene is used as an internal standard. We have shown previously that GPC purification leads to highly repeatable ligand populations, characterized by a single resolvable olefin peak in purified oleate-capped PbS QD samples below a critical size of ~5 nm, which includes those examined here.[23] Conversely, studies of PbS QDs purified with PR have indicated a diminishing ligand population with repeated PR cycles, attributed to dissociation of physisorbed materials and/or dissociation of lead oleate equivalents from weakly bound coordination sites: these changes can occur with a minimal effect on the electronic absorption spectrum.[12,40−42] The spectra for 3PR, 5PR, and GPC samples (Figure 1c) all show complete removal of residual octadecene growth solvent, unreacted precursors, and reaction byproducts and of narrow peaks associated with free or weakly associated oleate species. However, the bound surface ligand population per QD, as determined by integrating peaks for bound oleate in spectra to establish total ligand concentration and dividing by the QD

https://doi.org/10.1021/acs.jpcc.1c04218
J. Phys. Chem. C 2021, 125, 17796−17805

concentration from a UV−vis−NIR absorbance measurement, shows differences among the three samples. GPC QDs showed 348 OA/dot ligand population. The 3PR sample showed a slightly higher number, while 5PR cycles led to additional ligand loss down to ∼249 OA/dot. The lower number for 5PR could indicate bare sites, which could promote agglomeration. We note that close inspection of the UV−vis−NIR absorption spectra of solution-phase samples in Figure 1b shows a small red shift in the λ_{1s} peak after successive PR cycles. The ligand population determined for the GPC sample is in line with our previously determined ligand density versus size measurements for PbS QDs.[23] We also analyzed the purified QD sample by thermogravimetric analysis (TGA) and found that there was no significant difference in mass loss associated with decomposition of organic matter between the 3PR and GPC samples, consistent with comparable ligand populations among these two samples (Figure S3).

PbS QD films were formed through an air-free, layer-by-layer process. Spin coating of oleate-capped QDs was followed by ligand exchange with an EDT solution (Figure 1a). In particular, ∼100 nm-thick films were formed on Si/SiO_2 substrates. The efficacy of the ligand exchange process was confirmed by Fourier transform infrared (FTIR). The absence of C−H peaks around 3000 cm^{-1} indicates that the oleate ligand has been replaced by EDT (Figure S4).[43,44] The film thickness (Figure S5) and roughness (Figure 2) were measured by scanning electron microscopy (SEM) and atomic force microscopy (AFM). The overall morphology, as qualitatively seen under SEM imaging (Figure 2), is more uniform for GPC-purified QDs, with diminished incidence of micron-scale texture that is most evident in the 3PR sample. Localized surface roughness, measured by AFM, was comparable between 3PR and GPC but elevated in the 5PR sample, a possible consequence of partial agglomeration. After the layer-by-layer coating and exchange process, the films were dried by annealing in a glovebox overnight prior to contact formation. The UV−vis−NIR spectra of similar films deposited on glass substrates (Figure 1b) revealed an additional red shift of the lowest-energy exciton peak in all the three films, but with a greater shift for the PR films, as well as a sloping background characteristic of Rayleigh scattering. A red shift associated with increased delocalization and dielectric solvation in the presence of neighboring QDs can be anticipated on formation of close-packed QD films, but the greater red shift in the PR-purified vs GPC-purified films could be associated with ripening or aggregation.[45]

In order to directly characterize and compare the electronic properties of the PbS QD films, metal top contacts (pure Au for ohmic contacts and pure Al for Schottky contacts as discussed below) of 100 nm thickness were deposited through a shadow mask by electron beam evaporation. This process forms an intimate contact between the QD film and metals with reduced potential for the influence of surface relief, oxides, or organic residues that bottom contacts are susceptible to and similar concerns or mechanical damage that could result from traditional 4-point probe measurements. The evaporated metal films were contacted by fine W wires in a homebuilt probe station. All measurements were conducted under ambient conditions. As-fabricated devices were tested by current−voltage (I−V) measurement in the dark to obtain the resistivity and under monochromatic illumination to obtain the photocurrent action spectra. The responsivity was calibrated with an InGaAs commercial photodiode with known responsivity.

In a first set of measurements, we used a transmission line model (TLM) measurement approach, in which resistance is measured between pairs of neighboring, parallel contact stripes with increasing spacing, to measure separately the bulk film resistivity and the contact resistance.[46] Figure 3a shows the results for TLM patterns with width W = 4 mm, which is chosen to be at least 10× the maximum contact separation to minimize the influence of spreading resistance.

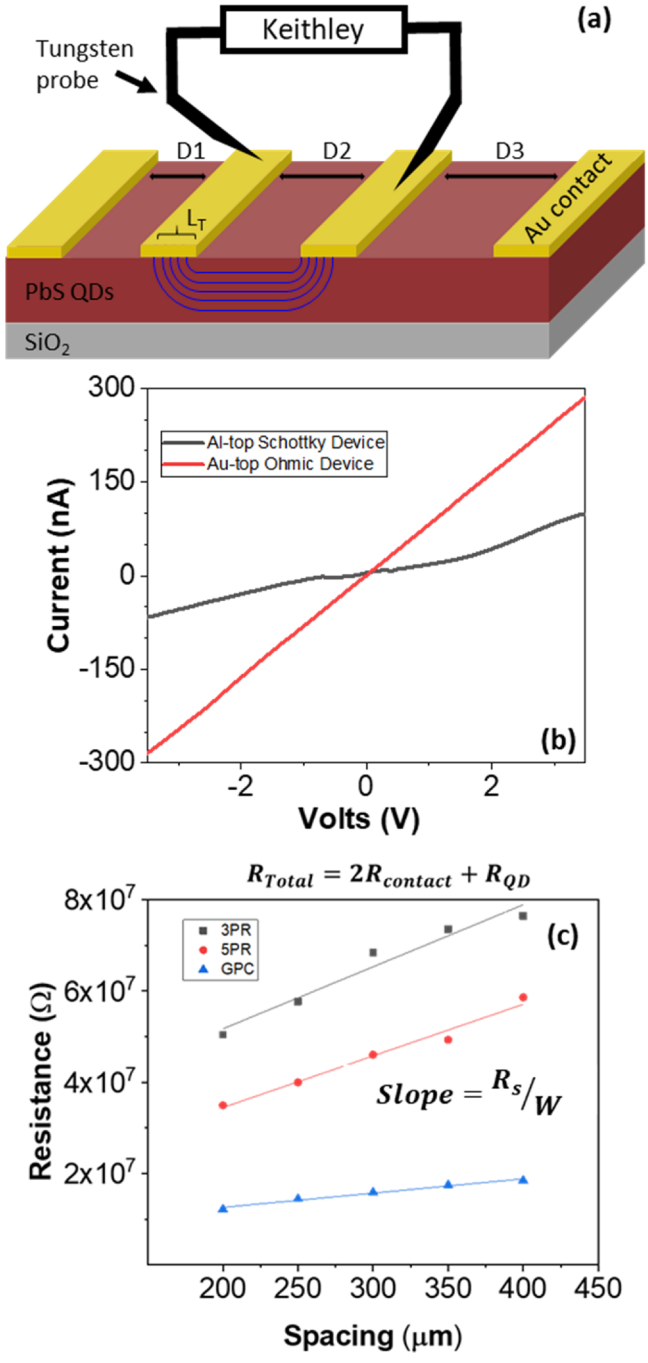

Figure 3. (a) Sketch of TLM devices indicating L_T. (b) I−V for ohmic and Schottky devices in the dark. (c) TLM results for sheet resistance and contact resistivity of EDT exchanged films on isolated Si/SiO_2 substrates.

https://doi.org/10.1021/acs.jpcc.1c04218
J. Phys. Chem. C 2021, 125, 17796−17805

Table 1. Electronic Properties of PbS-EDT Films Prepared following PR and GPC Purification

film	ligand/QD	resistivity (kΩ-cm)	$R_{C,sp}$ (kΩ-cm^2)	photocurrent lifetime, ohmic (ms)	μ ohmic (cm^2/Vs)	L_D (μm)	photocurrent lifetime, rectifying (ms)	μ_n, rectifying[a] (cm^2/Vs)
3PR	411	3.4 ± 0.4	18.0 ± 1.6	27	1.4×10^{-4}	15.1	0.296	2.9×10^{-1}
5PR	249	4.8 ± 0.0	16.8 ± 1.7	24	3.5×10^{-4}	15.3	0.252	3.6×10^{-1}
GPC	348	1.5 ± 0.4	5.9 ± 4.6	16	1.3×10^{-3}	15.8	0.119	8.1×10^{-1}

[a]Upper bound, based on eq 7.

The slope in these plots is nominally the resistance per unit length, equal to R_s/W, where R_s is the sheet resistance of the film, and the y-intercept is twice the contact resistance R_C. It is easily seen that the GPC film has the lowest sheet resistance, while all samples exhibited low contact resistance, consistent with the ohmic $I-V$ curves seen for Au contacts, as shown for a representative case in Figure 3b. As the film thickness is known, the bulk resistivity for the film can be obtained as

$$\rho = R_s d_{QD} \quad (1)$$

where d_{QD} is the film thickness. The product $R_C W$ gives a contact resistivity normalized by the width of the contact. Within the TLM formalism, for a film of uniform thickness, this contact resistivity can be interpreted arising from a specific contact resistance $R_{C,sp}$ for the metal/semiconductor interface. The specific contact resistance and film resistivity determine a characteristic distance over which current is transferred from the film to the top contact. This transfer length L_T can be read from (half) the x-intercept of the TLM plot, and from it, the specific contact resistance is obtained as

$$R_{C,sp} = R_C L_T W \quad (2)$$

The values of ρ for the QD films and $R_{C,sp}$ for the film/Au interface for 3PR, 5PR, and GPC samples, as established from measurements in triplicate on similarly prepared films, are listed in Table 1. We find that the GPC-purified film, despite a larger initial ligand/QD ratio than the 5PR sample, had the lowest resistivity (1.5 ± 0.4 kΩ-cm) and lowest contact resistance. The resistivity is comparable to the lowest values reported for PbS-EDT films prepared at room temperature (Table S2). The contact resistance, while small compared to the total resistance of the film, scales roughly with the resistivity, which has been observed previously in Au-contacted PbS QDs.[33]

In previous reports, EDT has been associated with a tendency to form QD films that have low binding energies for the valence band (band edges shifted to higher energy) and/or exhibit p-type conductivity, and Au has been routinely used to form ohmic contacts to EDT-capped PbS QD layers in solar cells.[47,36,48] The large workfunction of Au (ϕ = 5.1 eV) can be expected to lead to ohmic contacts to p-type semiconductors, but this is the first direct measurement of specific contact resistance for PbS QD films. We have previously noted ohmic contacts between EDT-capped PbS QD films and epitaxial graphene electrodes with a workfunction of ∼4.5 eV.[24] In contrast, we found that evaporated top contacts composed of Al, a low workfunction metal (ϕ = 4.3 eV), gave nonlinear $I-V$ curves (Figure 3b), indicative of contact barriers. In the case of the lateral metal−semiconductor−metal TLM structure, the two contacts are biased in opposite directions. However, rectifying behavior characteristic of a single p-type Schottky junction is seen when similarly prepared films are contacted with Al in a vertical transport geometry (Figure S6).

We investigated photoconductivity in the PbS QD films to evaluate the effective bandgap, photoconductive gain (g), and in order to evaluate whether the comparatively lower resistivity of the GPC-purified film arises from increased carrier concentration and/or increased carrier mobility. Figure 4b shows the representative photocurrent (I_{ph} vs V) characteristic for the three films with Au top contacts under wide-area illumination at 444 nm. Under 2.79 μW total power, the conductivity increases in all the three films and the photocurrent is approximately linear with power in this regime (Figure S7). The increase in conductivity is largest for the GPC-purified film.

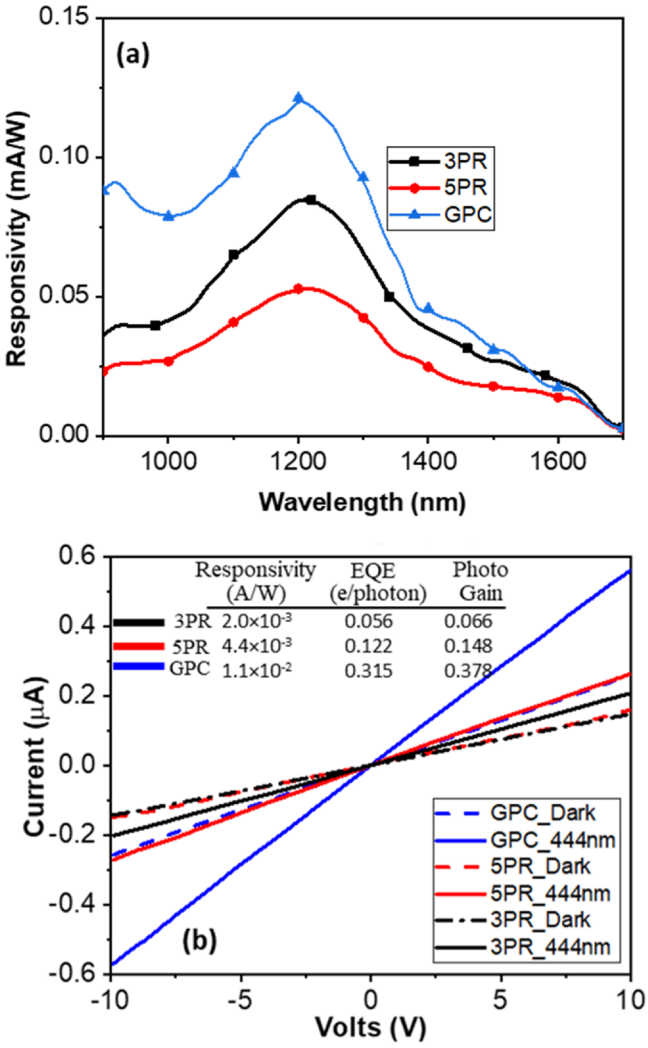

Figure 4. (a) Photocurrent action spectrum of films with ohmic contacts. (b) Dark and illuminated current of 75 μm × 200 μm Au-contacted (ohmic photoresistor devices at 2.79 μW 444 nm laser illumination.

https://doi.org/10.1021/acs.jpcc.1c04218
J. Phys. Chem. C 2021, 125, 17796−17805

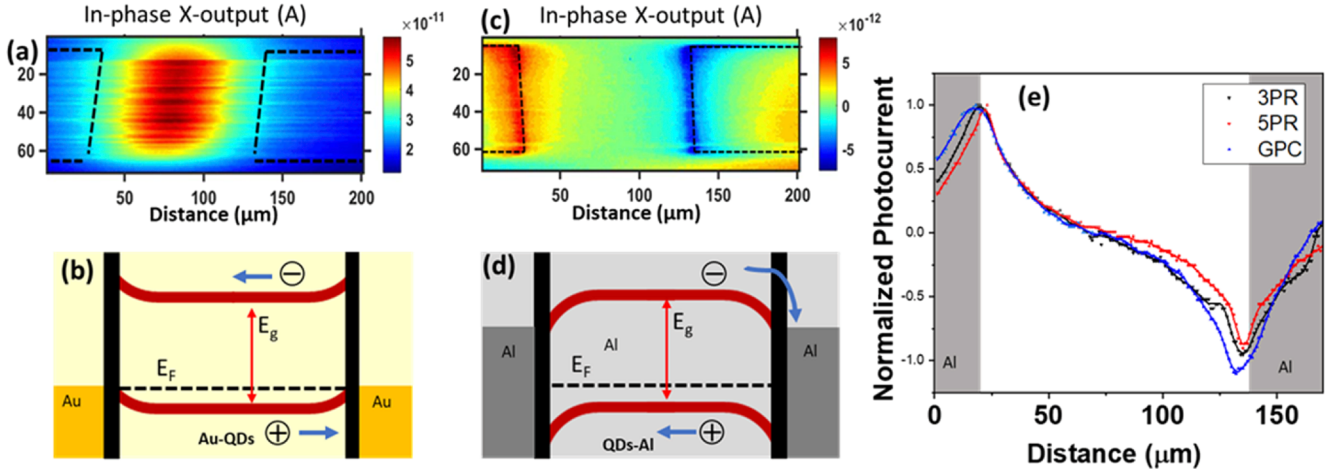

Figure 5. (a) SPCM of an ohmic (Au-electrodes) device and (b) respective energy band diagram. (c) SPCM of a Schottky (Al-electrodes) device and (d) respective energy band diagram. (e) Line scan photocurrent profiles for 3PR, 5PR, and GPC Schottky devices to extract diffusion length.

The linear increase in photocurrent with applied voltage in each case is a strong indicator of photoconductive gain. In a photoconductive sensor, the gain g (internal quantum efficiency) is determined by how many additional carriers can transit the device within the recombination lifetime.

From the directly measured responsivity R of such a device under monochromatic illumination, the external quantum efficiency (EQE) and photoconductive gain g can be obtained as

$$\mathrm{EQE} = \frac{R}{q}\frac{hc}{\lambda} = R\,E_{\mathrm{ph}} \tag{4}$$

$$g = \frac{\mathrm{EQE}}{1 - 10^{-A}} \tag{5}$$

where E_{ph} is the photon energy in eV and A is the absorbance of the film at the excitation wavelength, neglecting scattering and reflection. For this purpose, the film absorbance at 444 nm was directly measured using a confocal microscope and a calibrated photodiode detector in order to minimize any losses of transmitted light to small-angle scattering. The responsivity, EQE, and gain at a bias of 1 V for each of the devices studied in Figure 4 are shown in the inset table.

In general, the photoconductive gain can contain contributions from both electrons and holes:[49]

$$g = \frac{V}{L^2}(\mu_n + \mu_p)\tau_{\mathrm{rec}} = \frac{V}{L^2}\mu\tau_{\mathrm{rec}} \tag{3}$$

where μ_n and μ_p are the electron and hole mobilities, respectively, V is the applied voltage, and L is the length of the device in the direction of transport. On its own, the gain g of a device with known geometry provides an effective mobility−lifetime product $\mu\tau_{\mathrm{rec}}$ for the semiconductor material, where μ is the effective mobility (representing a sum of electron and hole mobilities). In practice, one carrier may become rapidly localized in low-mobility traps, in which case, $\mu\tau_{\mathrm{rec}}$ is determined by the more mobile carrier, which continues to cycle additional charges through the device until the ground state is recovered through recombination.

We found a $\mu\tau_{\mathrm{rec}}$ as high as 2.1×10^{-5} cm^2/V for the GPC-purified film. We note that this value exceeds mobility−lifetime products reported for holes[29,30,50] and electrons[51] in previous studies of PbS-EDT films, an indication of good quality, but additional information from time-resolved measurements below is needed to determine which carrier dominates the photoconductivity and principally determines the observed $\mu\tau_{\mathrm{rec}}$.

The photoresponse action spectrum (responsivity versus wavelength) of the GPC-purified films is shown in Figure 4a. The general shape is identical to the absorbance spectrum in Figure 1b, with the GPC responsivity comparable to the PR films near the band edge. The primary peak is slightly blue shifted for all the films with respect to the absorbance peak, a possible indication of enhanced exciton dissociation when smaller QDs are initially excited. Nonetheless, the action spectrum confirms that the photoconductivity is associated with the quantum confined effective bandgap and illustrates that those differences in responsivity for visible (444 nm) light are associated with a diminished response in the PR films at high photon energy, which could be associated with different rates for trapping and recombination upon thermalization of high-energy excited states.

Previously, researchers have measured μ using back-gated I−V measurements on field-effect transistor (FET) structures fabricated from QD films on SiO_2 dielectrics with conductive Si substrates serving as back gates, from which a field-effect mobility is extracted by assuming that the FET is biased in the triode region of the FET output characteristics, with a reported μ of ~10^{-3} cm^2/Vs for holes in PbS-EDT films.[32,52] However, the field-effect mobility may not accurately describe the behavior of charge-collecting devices due to limitations associated with carrier density, estimation of gate capacitance particularly in films that may experience compensation due to mobile ions or high trap density, and dependence of contact resistance on gate voltage near pinch-off.

To further analyze the optoelectronic properties of the PbS QD films and evaluate the barriers formed at low-workfunction metal contacts, we used scanning photocurrent microscopy (SPCM) to directly image charge collection and identify characteristic lengths.[24,33,36,53] This technique uses a focused, diffraction-limited light beam to locally create electron−hole pairs. The excitation spot is rastered over an electronic device to build a map of the resulting photocurrent as a function of the illumination position. SPCM was performed using 444 nm laser in a homebuilt setup described previously;[24,54] the laser modulation frequency was 71 Hz and the photocurrent

https://doi.org/10.1021/acs.jpcc.1c04218
J. Phys. Chem. C 2021, 125, 17796−17805

amplitude, along with the reflected light amplitude for spatial registry, was measured with lock-in detection. SPCM measurements were performed on devices formed between top contacts of smaller width than the TLM structures in order to increase the photocurrent relative to dark current under localized excitation.

Figure 5 illustrates the representative SPCM results for Au-contacted and Al-contacted devices, with otherwise identical design characteristics, prepared using the GPC-purified QDs. The bias V is held close to zero (short circuit) in each case. With Au contacts, the photocurrent signal has constant sign and reaches a maximum value between the contacts. This is consistent with photoconductive behavior in the presence of a small residual bias, in which diffusion of the lower-mobility carrier into the contacts diminishes the excitation lifetime compared to excitation at the center. Conversely, with Al contacts, the photocurrent displays an opposite sign (equivalently, a 180° phase shift) at the opposing contacts. The sign of the photocurrent near each contact indicates that localized excitation causes current flow from the Al contact into the PbS film, consistent with the photocurrent expected for a p-type Schottky barrier, reinforcing assignment of the p-type character for the PbS-EDT films studied here, consistent with previous reports. The magnitude of the photocurrent decreases slowly with distance away from each contact, falling to near zero in the center. The decay of photocurrent with distance is clearly much broader than the decay of the reflected signal: the reflected signal (shown in Figure S8) indicates the point spread function of the excitation laser beam that is convolved with the intrinsic response of the device. For a p-type Schottky contact, the distance over which charge can be collected is the depletion width plus the minority carrier diffusion length L_D. If L_D is long enough, electrons reach the metal electrode, and a photocurrent signal is observed. The photocurrent profiles shown in Figure 5e can thus be used to obtain L_D in the GPC, 3PR, and 5PR PbS-EDT films. The profiles in each case were well described by an exponential decay, indicating an electron diffusion length $L_D \approx 15$ μm (Figure S8). Previous SPCM investigations noted L_D larger than the film thickness, for example, up to ~1.7 μm for a film of 50 nm thickness. The thicker film and top contact geometry employed here may influence the considerably larger L_D observed here.

We performed transient photocurrent measurements in order to characterize the speed of the photoconductive and Schottky devices as sensors and also to enable estimation of the variation in carrier mobilities. The DC photoconductivity (with ohmic contacts) and SPCM results (with Schottky contacts) offer characteristic lengths for motion of the dominant carrier under drift (as $\mu\tau_{rec} \times V/L$) and for motion of minority carriers under diffusion (L_D), respectively. By combining these with lifetimes, mobility values can be obtained. For the Schottky case

$$L_D = \sqrt{D\tau_n} = \sqrt{\frac{k_B T}{q}\mu_n \tau_n} \tag{6}$$

$$\mu_n = \frac{q}{k_B T}\frac{L_D^2}{\tau_n} \tag{7}$$

with τ_n being the electron lifetime in the conduction band.

Figure 6 shows the transient decays for ohmic-contacted (a) and Schottky-contacted (b) films. All decays were collected by using a digital oscilloscope to monitor the falling edge of the current signal when the device was excited with a 5 Hz square-wave modulated, wide-area laser beam. The data were collected at a constant bias of 3 V to ensure a high-enough signal to noise ratio.

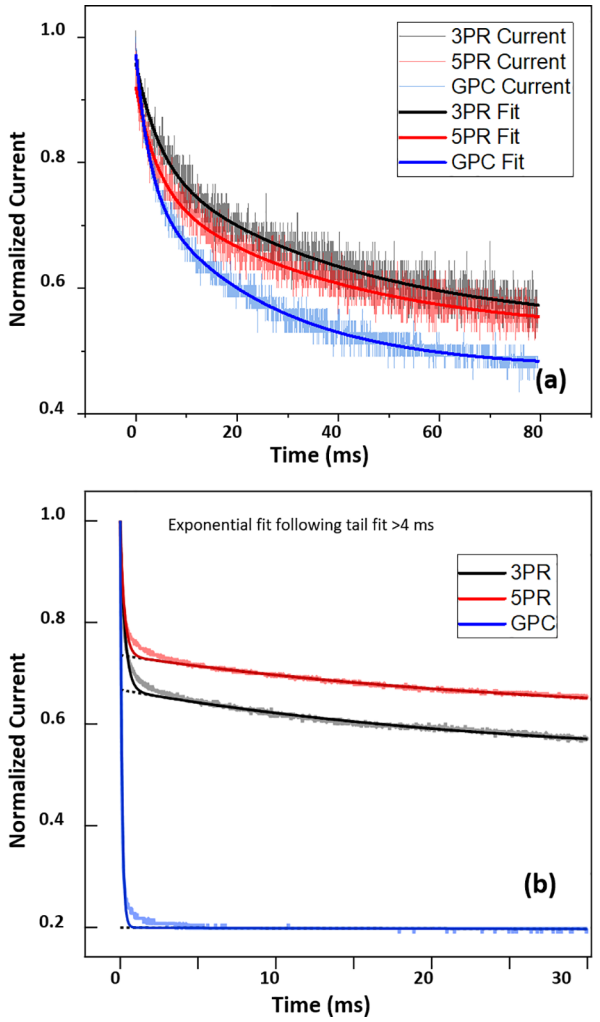

Figure 6. Transient photocurrent decays for (a) Au-contacted (ohmic) and (b) Al-contacted (Schottky) PbS QD films. Fit lines represent biexponentials as described in text.

The ohmic-contacted films all showed photocurrent decays over tens of milliseconds with multiexponential line shapes. As shown in Table 1, the average lifetime for the GPC-purified films (16 ms) was shorter than that for 3PR or 5PR (multiexponential analysis is detailed in Table S1).

For the Schottky-contacted devices, the transient photocurrent decay represents the characteristic time required for photoexcited minority carriers (electrons) to recombine or be swept out of the device. As such, the measured lifetime is a lower limit on τ_n and the recombination time τ_{rec}. All devices showed a fast, sub-millisecond decay that was accompanied, in the PR cases, by a longer decay component with a lifetime of >20 ms. By separately fitting the slow (>4 ms) and fast (<4 ms) components of the response, it is clear that the slow component is absent in the GPC films. We used tail fitting for transient photocurrent decays to separate out fast and slow components and used a single-parameter fit of the fast component lifetime to evaluate differences in minority carrier mobility based on eq 7 since the slow component is effectively filtered out in SPCM. The fast component, which dominates

https://doi.org/10.1021/acs.jpcc.1c04218
J. Phys. Chem. C 2021, 125, 17796−17805

the response at the 71 Hz frequency used for SPCM imaging, was significantly faster in the GPC film compared to the PR examples, as indicated in Table 1. The shorter lifetime in the GPC-purified films, together with a comparable diffusion length, is consistent with an electron mobility μ_n that is also higher in the GPC-purified films than for PR.

Returning to the behavior of the ohmically contacted devices, we note that the photocurrent decay in these devices is much slower than the decay time for electrons in the Schottky-contacted devices, suggesting that electrons are significantly trapped on a sub-millisecond timescale, and the photoconductive gain seen with Au contacts is dominated by holes. For a *p*-type film, the low Fermi level position will tend to expose electron traps. If holes dominate the photoconductivity, the observed $\mu\tau_{rec}$ can be used to assign the hole mobility μ_p, which when combined with the observed dark conductivity, provides an estimate of the hole concentration as $p = (q\mu_p\rho)^{-1}$, giving a p of $\sim 10^{18}$ cm^{-3} for the three films examined here. The 5PR and GPC films had comparable hole concentrations, with the improved performance of the GPC film arising from significantly greater mobility. The 3PR film showed the lowest mobility; its conductivity, being comparable to the 5PR case, is driven by an elevated hole concentration that could arise from a greater surface area exposed to air via micron-scale texture seen in SEM. Overall, the hole densities are comparable to $1-2 \times 10^{18}$ cm^{-3} reported from field-effect measurements on larger (8.8 nm) PbS QD films[47] prepared by layer-by-layer ligand exchange with short-chain carboxylates (Table S2).

The mobility values obtained in the ohmic- and Schottky-contacted cases are not directly comparable head-to-head, as they are obtained under different measurement conditions, but they can be used to compare samples prepared and measured similarly, as in the case here among 3PR, 5PR, and GPC-purified films. The photoconductive gain is measured under wide-area illumination in ohmic devices, while the diffusion length L_D is measured under focused illumination in rectifying devices, with locally higher power density. Nonetheless, the higher electron mobilities calculated from the Schottky device results may indicate a significant contribution of electrons to the effective mobility observed in ohmically contacted devices.

CONCLUSIONS

In this study, we have utilized variable contact spacing, time-resolved photocurrent, and SPCM to analyze charge transport in films of uniform thickness prepared from purified PbS QDs with known ligand populations. GPC purification provided lower resistivity, lower contact resistance, higher photoconductive gain, and shorter lifetimes than PR purification. An effective mobility−lifetime product of an order of magnitude greater than those of previously studied PbS QD films is obtained using the GPC-purified QD sample.[50] Meanwhile, an electron diffusion length of >10 μm was observed via the SPCM profile near a rectifying *p*-type Schottky barrier. Transient photocurrent measurements on the Schottky-contacted devices revealed a much shorter lifetime in the GPC-purified case, indicating a higher electron mobility. These results emphasize a role for detailed control of QD surfaces in improving the response time of QD-based IR photodetectors. While the emphasis of the present study has been on comparing film's electronic properties, identifying the chemical and physical origins of the differences observed will help to improve the performance and durability of SSLE QD solids. Microscale roughness and spectroscopic red shift point to aggregation as a limitation when PR is carried out in excess, while larger-scale cracks may introduce additional scattering and elevated carrier densities on air exposure. Among the purified QD samples, there was no case where significant impurity concentrations were detected by NMR to impact film properties. The ligand density of the GPC sample fell between those of the PR films examined here, but the presence of long-lived photocurrent decay in Schottky contacts to both PR films, absent in the GPC case, suggests that the performance is not simply a matter of optimizing residual ligand density and that differences in solvent exposure or interparticle contact during purification are possible drivers of variation in electronic properties following SSLE in PbS QD films.

ASSOCIATED CONTENT

Supporting Information

The Supporting Information is available free of charge at https://pubs.acs.org/doi/10.1021/acs.jpcc.1c04218.

Detailed information on materials and synthesis, UV−vis−NIR absorbance spectrum for QDs in solution and films, thermogravimetric analysis (TGA), ATR-FTIR spectra of spin-cast PbS QD films, SEM images of thin films, *I*−*V* curve for the Al/PbS-EDT Schottky diode, intensity-dependent photocurrent response, SPCM photocurrent and reflected signals, and tables of transient photocurrent fit parameters and literature reference values (Figures S1−S8 and Tables S1 and S2) (PDF)

AUTHOR INFORMATION

Corresponding Author

Andrew B. Greytak − *Department of Chemistry and Biochemistry, University of South Carolina, Columbia, South Carolina 29208, United States;* orcid.org/0000-0001-8978-6457; Email: greytak@sc.edu

Authors

Fiaz Ahmed − *Department of Chemistry and Biochemistry, University of South Carolina, Columbia, South Carolina 29208, United States;* orcid.org/0000-0002-6977-3672

Mathew L. Kelley − *Department of Chemistry and Biochemistry, University of South Carolina, Columbia, South Carolina 29208, United States;* orcid.org/0000-0002-6940-4148

MVS Chandrashekhar − *Department of Electrical and Computer Engineering, University of South Carolina, Columbia, South Carolina 29208, United States*

Complete contact information is available at: https://pubs.acs.org/10.1021/acs.jpcc.1c04218

Notes

The authors declare no competing financial interest.

ACKNOWLEDGMENTS

This project has been partially supported by the National Science Foundation (NSF), through ECCS award no. 1711322. M.L.K. was additionally supported by an NSF IGERT graduate fellowship under grant no. 1250052. The authors also acknowledge support from the University of South Carolina through the ASPIRE program. We thank Drs. Adam

Roberge, Bobby G. Barker, Jr., and Perry J. Pellechia for helpful discussions.

REFERENCES

(1) Konstantatos, G.; Sargent, E. H. *Colloidal Quantum Dot Optoelectronics and Photovoltaics*; Cambridge University Press, 2013.

(2) De Iacovo, A.; Venettacci, C.; Colace, L.; Scopa, L.; Foglia, S. PbS Colloidal Quantum Dot Photodetectors Operating in the near Infrared. *Sci. Rep.* **2016**, *6*, 37913.

(3) Kim, G.-H.; García de Arquer, F. P.; Yoon, Y. J.; Lan, X.; Liu, M.; Voznyy, O.; Yang, Z.; Fan, F.; Ip, A. H.; Kanjanaboos, P.; Hoogland, S.; Kim, J. Y.; Sargent, E. H. High-Efficiency Colloidal Quantum Dot Photovoltaics via Robust Self-Assembled Monolayers. *Nano Lett.* **2015**, *15*, 7691−7696.

(4) Kagan, C. R.; Lifshitz, E.; Sargent, E. H.; Talapin, D. V. Building Devices from Colloidal Quantum Dots. *Science* **2016**, *353*, No. aac5523.

(5) de Arquer, F. P. G.; Armin, A.; Meredith, P.; Sargent, E. H. Solution-Processed Semiconductors for next-Generation Photodetectors. *Nat. Rev. Mater.* **2017**, *2*, 16100.

(6) Kagan, C. R.; Murray, C. B. Charge Transport in Strongly Coupled Quantum Dot Solids. *Nat. Nanotechnol.* **2015**, *10*, 1013.

(7) Moreels, I.; Justo, Y.; De Geyter, B.; Haustraete, K.; Martins, J. C.; Hens, Z. Size-Tunable, Bright, and Stable PbS Quantum Dots: A Surface Chemistry Study. *ACS Nano* **2011**, *5*, 2004−2012.

(8) Ellingson, R. J.; Beard, M. C.; Johnson, J. C.; Yu, P.; Micic, O. I.; Nozik, A. J.; Shabaev, A.; Efros, A. L. Highly Efficient Multiple Exciton Generation in Colloidal PbSe and PbS Quantum Dots. *Nano Lett.* **2005**, *5*, 865−871.

(9) Konstantatos, G.; Sargent, E. H. Solution-Processed Quantum Dot Photodetectors. *Proc. IEEE* **2009**, *97*, 1666−1683.

(10) Wang, R.; Shang, Y.; Kanjanaboos, P.; Zhou, W.; Ning, Z.; Sargent, E. H. Colloidal Quantum Dot Ligand Engineering for High Performance Solar Cells. *Energy Environ. Sci.* **2016**, *9*, 1130−1143.

(11) Lin, Q.; Yun, H. J.; Liu, W.; Song, H.-J.; Makarov, N. S.; Isaienko, O.; Nakotte, T.; Chen, G.; Luo, H.; Klimov, V. I.; Pietryga, J. M. Phase-Transfer Ligand Exchange of Lead Chalcogenide Quantum Dots for Direct Deposition of Thick, Highly Conductive Films. *J. Am. Chem. Soc.* **2017**, *139*, 6644−6653.

(12) Ip, A. H.; Thon, S. M.; Hoogland, S.; Voznyy, O.; Zhitomirsky, D.; Debnath, R.; Levina, L.; Rollny, L. R.; Carey, G. H.; Fischer, A.; Kemp, K. W.; Kramer, I. J.; Ning, Z.; Labelle, A. J.; Chou, K. W.; Amassian, A.; Sargent, E. H. Hybrid Passivated Colloidal Quantum Dot Solids. *Nat. Nanotechnol.* **2012**, *7*, 577.

(13) Oh, S. J.; Straus, D. B.; Zhao, T.; Choi, J.-H.; Lee, S.-W.; Gaulding, E. A.; Murray, C. B.; Kagan, C. R. Engineering the Surface Chemistry of Lead Chalcogenide Nanocrystal Solids to Enhance Carrier Mobility and Lifetime in Optoelectronic Devices. *Chem. Commun.* **2017**, *53*, 728−731.

(14) King, L. A.; Riley, D. J. Importance of QD Purification Procedure on Surface Adsorbance of QDs and Performance of QD Sensitized Photoanodes. *J. Phys. Chem. C* **2012**, *116*, 3349−3355.

(15) Sambur, J. B.; Riha, S. C.; Choi, D.; Parkinson, B. A. Influence of Surface Chemistry on the Binding and Electronic Coupling of CdSe Quantum Dots to Single Crystal TiO_2 Surfaces. *Langmuir* **2010**, *26*, 4839−4847.

(16) Shen, Y.; Tan, R.; Gee, M. Y.; Greytak, A. B. Quantum Yield Regeneration: Influence of Neutral Ligand Binding on Photophysical Properties in Colloidal Core/Shell Quantum Dots. *ACS Nano* **2015**, *9*, 3345−3359.

(17) Shakeri, B.; Meulenberg, R. W. A Closer Look into the Traditional Purification Process of CdSe Semiconductor Quantum Dots. *Langmuir* **2015**, *31*, 13433−13440.

(18) Morris-Cohen, A. J.; Donakowski, M. D.; Knowles, K. E.; Weiss, E. A. The Effect of a Common Purification Procedure on the Chemical Composition of the Surfaces of CdSe Quantum Dots Synthesized with Trioctylphosphine Oxide. *J. Phys. Chem. C* **2010**, *114*, 897−906.

(19) Kim, T.; Kelley, M. L.; Kim, D.; Greytak, A. B.; Jeong, S. Purification of Colloidal Nanocrystals Along the Road to Highly Efficient Photovoltaic Devices. *Int. J. Precis. Eng. and Manuf.-Green Technol.* **2021**, *8*, 1309−1321.

(20) Shcherbakov-Wu, W.; Tisdale, W. A. A Time-Domain View of Charge Carriers in Semiconductor Nanocrystal Solids. *Chem. Sci.* **2020**, *11*, 5157−5167.

(21) Shen, Y.; Gee, M. Y.; Tan, R.; Pellechia, P. J.; Greytak, A. B. Purification of Quantum Dots by Gel Permeation Chromatography and the Effect of Excess Ligands on Shell Growth and Ligand Exchange. *Chem. Mater.* **2013**, *25*, 2838−2848.

(22) Shen, Y.; Gee, M. Y.; Greytak, A. B. Purification Technologies for Colloidal Nanocrystals. *Chem. Commun.* **2017**, *53*, 827−841.

(23) Roberge, A.; Dunlap, J. H.; Ahmed, F.; Greytak, A. B. Size-Dependent PbS Quantum Dot Surface Chemistry Investigated via Gel Permeation Chromatography. *Chem. Mater.* **2020**, *32*, 6588−6594.

(24) Kelley, M. L.; Letton, J.; Simin, G.; Ahmed, F.; Love-Baker, C. A.; Greytak, A. B.; Chandrashekhar, M. V. S. Photovoltaic and Photoconductive Action Due to PbS Quantum Dots on Graphene/SiC Schottky Diodes from NIR to UV. *ACS Appl. Electron. Mater.* **2020**, *2*, 134−139.

(25) Weidman, M. C.; Yager, K. G.; Tisdale, W. A. Interparticle Spacing and Structural Ordering in Superlattice PbS Nanocrystal Solids Undergoing Ligand Exchange. *Chem. Mater.* **2015**, *27*, 474−482.

(26) Talapin, D. V.; Lee, J.-S.; Kovalenko, M. V.; Shevchenko, E. V. Prospects of Colloidal Nanocrystals for Electronic and Optoelectronic Applications. *Chem. Rev.* **2010**, *110*, 389−458.

(27) Song, J. H.; Jeong, S. Colloidal Quantum Dot Based Solar Cells: From Materials to Devices. *Nano Convergence* **2017**, *4*, 21.

(28) Klem, E. J. D.; Shukla, H.; Hinds, S.; MacNeil, D. D.; Levina, L.; Sargent, E. H. Impact of Dithiol Treatment and Air Annealing on the Conductivity, Mobility, and Hole Density in PbS Colloidal Quantum Dot Solids. *Appl. Phys. Lett.* **2008**, *92*, 212105.

(29) Johnston, K. W.; Pattantyus-Abraham, A. G.; Clifford, J. P.; Myrskog, S. H.; Hoogland, S.; Shukla, H.; Klem, E. J. D.; Levina, L.; Sargent, E. H. Efficient Schottky-Quantum-Dot Photovoltaics: The Roles of Depletion, Drift, and Diffusion. *Appl. Phys. Lett.* **2008**, *92*, 122111.

(30) Rath, A. K.; Lasanta, T.; Bernechea, M.; Diedenhofen, S. L.; Konstantatos, G. Determination of Carrier Lifetime and Mobility in Colloidal Quantum Dot Films via Impedance Spectroscopy. *Appl. Phys. Lett.* **2014**, *104*, No. 063504.

(31) Kwan Kim, J.; Hoon Song, J.; Choi, H.; Jae Baik, S.; Jeong, S. Space Charge Limited Conduction in Ultrathin PbS Quantum Dot Solid Diodes. *J. Appl. Phys.* **2014**, *115*, No. 054302.

(32) Cao, Y.; Stavrinadis, A.; Lasanta, T.; So, D.; Konstantatos, G. The Role of Surface Passivation for Efficient and Photostable PbS Quantum Dot Solar Cells. *Nat. Energy* **2016**, *1*, 1−6.

(33) Kim, Y.; Cho, S.; Jeong, S.; Ko, D.-H.; Ko, H.; You, N.; Chang, M.; Reichmanis, E.; Park, J.-Y.; Park, S. Y.; et al. Competition between Charge Transport and Energy Barrier in Injection-Limited Metal/Quantum Dot Nanocrystal Contacts. *Chem. Mater.* **2014**, *26*, 6393−6400.

(34) Lai, Y.; Li, H.; Kim, D. K.; Diroll, B. T.; Murray, C. B.; Kagan, C. R. Low-Frequency (1/f) Noise in Nanocrystal Field-Effect Transistors. *ACS Nano* **2014**, *8*, 9664−9672.

(35) Otto, T.; Miller, C.; Tolentino, J.; Liu, Y.; Law, M.; Yu, D. Gate-Dependent Carrier Diffusion Length in Lead Selenide Quantum Dot Field-Effect Transistors. *Nano Lett.* **2013**, *13*, 3463−3469.

(36) Strasfeld, D. B.; Dorn, A.; Wanger, D. D.; Bawendi, M. G. Imaging Schottky Barriers and Ohmic Contacts in PbS Quantum Dot Devices. *Nano Lett.* **2012**, *12*, 569−575.

(37) Zhang, J.; Crisp, R. W.; Gao, J.; Kroupa, D. M.; Beard, M. C.; Luther, J. M. Synthetic Conditions for High-Accuracy Size Control of PbS Quantum Dots. *J. Phys. Chem. Lett.* **2015**, *6*, 1830−1833.

(38) Shen, Y.; Roberge, A.; Tan, R.; Gee, M. Y.; Gary, D. C.; Huang, Y.; Blom, D. A.; Benicewicz, B. C.; Cossairt, B. M.; Greytak, A. B. Gel Permeation Chromatography as a Multifunctional Processor for

https://doi.org/10.1021/acs.jpcc.1c04218
J. Phys. Chem. C 2021, 125, 17796−17805

Nanocrystal Purification and On-Column Ligand Exchange Chemistry. *Chem. Sci.* **2016**, *7*, 5671−5679.
(39) De Roo, J.; Yazdani, N.; Drijvers, E.; Lauria, A.; Maes, J.; Owen, J. S.; Van Driessche, I.; Niederberger, M.; Wood, V.; Martins, J. C.; Infante, I.; Hens, Z. Probing Solvent−Ligand Interactions in Colloidal Nanocrystals by the NMR Line Broadening. *Chem. Mater.* **2018**, *30*, 5485−5492.
(40) Weir, M. P.; Toolan, D. T. W.; Kilbride, R. C.; Penfold, N. J. W.; Washington, A. L.; King, S. M.; Xiao, J.; Zhang, Z.; Gray, V.; Dowland, S.; et al. Ligand Shell Structure in Lead Sulfide−Oleic Acid Colloidal Quantum Dots Revealed by Small-Angle Scattering. *J. Phys. Chem. Lett.* **2019**, *10*, 4713−4719.
(41) Kessler, M. L.; Dempsey, J. L. Mapping the Topology of PbS Nanocrystals through Displacement Isotherms of Surface-Bound Metal Oleate Complexes. *Chem. Mater.* **2020**, *32*, 2561−2571.
(42) Tang, J.; Kemp, K. W.; Hoogland, S.; Jeong, K. S.; Liu, H.; Levina, L.; Furukawa, M.; Wang, X.; Debnath, R.; Cha, D.; et al. Colloidal-Quantum-Dot Photovoltaics Using Atomic-Ligand Passivation. *Nat. Mater.* **2011**, *10*, 765−771.
(43) Kuo, C.-Y.; Su, M.-S.; Ku, C.-S.; Wang, S.-M.; Lee, H.-Y.; Wei, K.-H. Ligands Affect the Crystal Structure and Photovoltaic Performance of Thin Films of PbSe Quantum Dots. *J. Mater. Chem.* **2011**, *21*, 11605−11612.
(44) Yang, Z.; Fan, J. Z.; Proppe, A. H.; de Arquer, F. P. G.; Rossouw, D.; Voznyy, O.; Lan, X.; Liu, M.; Walters, G.; Quintero-Bermudez, R.; Sun, B.; Hoogland, S.; Botton, G. A.; Kelley, S. O.; Sargent, E. H. Mixed-Quantum-Dot Solar Cells. *Nat. Commun.* **2017**, *8*, 1325.
(45) Kirmani, A. R.; Walters, G.; Kim, T.; Sargent, E. H.; Amassian, A. Optimizing Solid-State Ligand Exchange for Colloidal Quantum Dot Optoelectronics: How Much Is Enough? *ACS Appl. Energy Mater.* **2020**, *3*, 5385−5392.
(46) Schroder, D. K. *Semiconductor Material and Device Characterization*; John Wiley & Sons, 2015.
(47) Zarghami, M. H.; Liu, Y.; Gibbs, M.; Gebremichael, E.; Webster, C.; Law, M. P-Type PbSe and PbS Quantum Dot Solids Prepared with Short-Chain Acids and Diacids. *ACS Nano* **2010**, *4*, 2475−2485.
(48) Chuang, C.-H. M.; Brown, P. R.; Bulović, V.; Bawendi, M. G. Improved Performance and Stability in Quantum Dot Solar Cells through Band Alignment Engineering. *Nat. Mater.* **2014**, *13*, 796−801.
(49) Singh, J. *Optoelectronics: An Introduction to Materials and Devices*; McGraw-Hill College, 1996.
(50) Jeong, K. S.; Tang, J.; Liu, H.; Kim, J.; Schaefer, A. W.; Kemp, K.; Levina, L.; Wang, X.; Hoogland, S.; Debnath, R.; et al. Enhanced Mobility-Lifetime Products in PbS Colloidal Quantum Dot Photovoltaics. *ACS Nano* **2012**, *6*, 89−99.
(51) Tang, J.; Brzozowski, L.; Barkhouse, D. A. R.; Wang, X.; Debnath, R.; Wolowiec, R.; Palmiano, E.; Levina, L.; Pattantyus-Abraham, A. G.; Jamakosmanovic, D.; et al. Quantum Dot Photovoltaics in the Extreme Quantum Confinement Regime: The Surface-Chemical Origins of Exceptional Air- and Light-Stability. *ACS Nano* **2010**, *4*, 869−878.
(52) Bederak, D.; Balazs, D. M.; Sukharevska, N. V.; Shulga, A. G.; Abdu-Aguye, M.; Dirin, D. N.; Kovalenko, M. V.; Loi, M. A. Comparing Halide Ligands in PbS Colloidal Quantum Dots for Field-Effect Transistors and Solar Cells. *ACS applied nano materials* **2018**, *1*, 6882−6889.
(53) Graham, R.; Yu, D. Scanning Photocurrent Microscopy in Semiconductor Nanostructures. *Mod. Phys. Lett. B* **2013**, *27*, 1330018.
(54) Barker, B. G., Jr.; Chava, V. S. N.; Daniels, K. M.; Chandrashekhar, M. V. S.; Greytak, A. B. Sub-Bandgap Response of Graphene/SiC Schottky Emitter Bipolar Phototransistor Examined by Scanning Photocurrent Microscopy. *2D Mater.* **2018**, *5*, No. 011003.

https://doi.org/10.1021/acs.jpcc.1c04218
J. Phys. Chem. C 2021, 125, 17796−17805